

Radio science measurements of atmospheric refractivity with Mars Global Surveyor

K. L. Cahoy,¹ D. P. Hinson,¹ and G. L. Tyler¹

Received 9 November 2005; revised 10 January 2006; accepted 27 January 2006; published 19 May 2006.

[1] Radio occultation experiments with Mars Global Surveyor measure the refractive index of the Martian atmosphere from the surface to ~ 250 km in geopotential height. Refractivity is proportional to neutral density at low altitudes and electron density at high altitudes, with a transition at ~ 75 km. We use weighted least squares to decompose zonal refractivity variations into amplitudes and phases for observed wave numbers $k = 1-4$ over the entire altitude range and use the results to analyze atmospheric structure and dynamics. The data set consists of 147 refractivity profiles acquired in December 2000 at summer solstice in the Martian northern hemisphere. The measurements are at an essentially fixed local time (sunrise) and at latitudes from 67° to 70° N. Thermal tides appear to be responsible for much of the observed ionospheric structure from 80 to 220 km. Tides modulate the neutral density, which in turn, controls the height at which the ionosphere forms. The resulting longitude-dependent vertical displacement of the ionosphere generates distinctive structure in the fitted amplitudes, particularly at $k = 3$, within ± 50 km of the electron density peak height. Our $k = 3$ observations are consistent with an eastward propagating semidiurnal tide with zonal wave number 1. Relative to previous results, our analysis extends the characterization of tides to altitudes well above and below the electron density peak. In the neutral atmosphere, refractivity variations from the surface to 50 km appear to arise from stationary Rossby waves. Upon examining the full vertical range, stationary waves appear to dominate altitudes below ~ 75 km, and thermal tides dominate altitudes above this transition region.

Citation: Cahoy, K. L., D. P. Hinson, and G. L. Tyler (2006), Radio science measurements of atmospheric refractivity with Mars Global Surveyor, *J. Geophys. Res.*, *111*, E05003, doi:10.1029/2005JE002634.

1. Introduction

[2] Since January 1998, Mars Global Surveyor (MGS) has performed over 17,000 radio occultation experiments, each sounding the atmosphere of Mars from the surface to ~ 250 km. These measurements are converted to profiles of refractivity via the Abel transform [Fjeldbo *et al.*, 1971]. Because refractivity is sensitive to both the neutral atmosphere and the charged particles in the ionosphere, two subset data products can be derived from the source profiles [Hinson *et al.*, 1999]. In the neutral atmosphere, profiles of temperature and pressure versus geopotential extend from the surface through ~ 40 km, where the data become too noisy to be integrated reliably and consistently. In the ionosphere, electron density profiles extend from ~ 100 to 200 km. Both subsets of profiles are typically produced with a vertical resolution of about 500 m.

[3] Figure 1 summarizes the altitude coverage of the Martian atmosphere by MGS experiments and relevant Mars global circulation models (MGCs). From Figure 1

it is clear that the radio science refractivity measurements, in their entirety, nearly double the altitude coverage of the temperature, pressure, and electron density profiles.

[4] Significant discoveries have been made using the MGS radio science profiles. For example, the high vertical resolution radio science temperature and pressure profiles, in conjunction with MGC simulations, allowed detailed analysis of the structure and dynamics in the lower atmosphere [e.g., Hinson and Wilson, 2004; Hinson *et al.*, 2003]. Radio science electron density profiles were used to study the interannual variability of the ionosphere, the interaction between the neutral atmosphere and the ionosphere, the role of tides in the ionosphere [e.g., Bougher *et al.*, 2001, 2004], and the effects of crustal magnetic fields on the ionosphere [e.g., Krymskii *et al.*, 2003; Withers *et al.*, 2005].

[5] Previous studies using the other MGS experimental data sets mentioned in Figure 1 have contributed substantially to the understanding of structure and dynamics in the Martian atmosphere. The MGS Thermal Emission Spectrometer (TES) nadir measurements cover approximately the same 0–40 km range as the radio occultation-derived temperature and pressure profiles, and the two compare well against each other [Hinson *et al.*, 2004]. More than two Martian years of TES measurements have been used to study both the interannual variability and the seasonal dependency of atmospheric parameters such as temperature,

¹Department of Electrical Engineering, Stanford University, Stanford, California, USA.

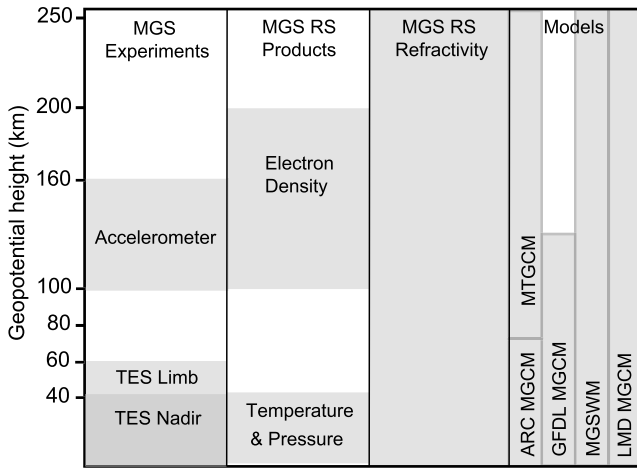


Figure 1. Vertical range of data products from selected Mars atmospheric experiments and numerical models. The set of MGS experiments includes TES nadir and limb profiles, accelerometer density measurements, and radio science profiles of temperature, pressure, electron density, and refractivity. Numerical models include the LMD MGCM [Forget et al., 1999; Angelats i Coll et al., 2005] as well as the Mars thermospheric general circulation model (MTGCM) [Bougher et al., 1999, 2000], the Mars global scale wave model (MGSWM) [Forbes and Hagan, 2000], the Geophysical Fluid Dynamics Laboratory (GFDL) MGCM [Wilson and Hamilton, 1996], and the NASA Ames Research Center (ARC) MGCM [Pollack et al., 1990]. Altitude ranges are approximate. The stacking of the ARC MGCM and MTGCM indicates potential coupling between the models to achieve a larger coverage in altitude [Bougher et al., 2004].

dust and water ice opacity, and water vapor column abundance [Smith et al., 2001a; Smith, 2004]. TES nadir data are also used in studies of stationary waves, thermal tides, traveling waves, and regions of instability [Banfield et al., 2003, 2004]. Although TES limb observations extend to a higher altitude than TES nadir measurements, the limb measurements have lower horizontal resolution and less complete spatial coverage than the nadir measurements. TES limb data have been used to study water ice clouds [Pearl et al., 2001], thermal structure and gradient winds [Smith et al., 2001b], and stationary Rossby waves [Hinson et al., 2003].

[6] MGS accelerometer density measurements were made during aerobraking at ~ 110 – 160 km and overlap the radio occultation electron density profiles in altitude coverage. Stationary density structures with longitude were observed in the MGS accelerometer measurements [Keating et al., 1998], and attributed to thermal tides after comparison with MGCM simulations [Forbes and Hagan, 2000; Wilson, 2002; Forbes et al., 2002]. The accelerometer measurements were analyzed further using classical tidal theory to identify dominant tidal modes; this analysis supported and extended the MGCM results [Withers et al., 2003]. Accelerometer density measurements at ~ 115 km were also recently compared with the MGCM from the Laboratoire de Météorologie Dynamique (LMD) to identify dominant

tidal components and to test the effects of near infrared tidal forcing [Angelats i Coll et al., 2004]. We note that the LMD MGCM has recently been extended to 240 km so that it now covers the full range of the MGS refractivity profiles [Angelats i Coll et al., 2005; Gonzalez-Galindo et al., 2005].

[7] Computational models mentioned in Figure 1 that are currently more restricted in altitude have successfully employed coupling techniques to study a larger altitude range and investigate density variation and interactions between the lower and upper regions of the Martian atmosphere [e.g., Forbes et al., 2002; Bougher et al., 2004].

[8] In this paper, we demonstrate that the MGS refractivity profiles provide new information about Martian atmospheric structure over the entire altitude range of the radio science experiment. After describing our approach, which employs a weighted least squares wave decomposition of zonal refractivity variation, we present results from the neutral atmosphere through the ionosphere. The wave decomposition allows us to examine the amplitude and phase of each observed wave number as well as their composite sum from the surface through 250 km. Our refractivity results support and extend previous results from other experiments and simulations at the same latitude and season as the data set used in this work.

2. Observations

[9] The 147 refractivity profiles used in this analysis were acquired during the period 9–21 December 2000. This data set spans the summer solstice in the Martian northern hemisphere, ranging from 87 to 92° in L_S . The measurements were obtained at essentially fixed local solar time, with t_{LST} ranging from 2.76 to 2.79 hours, and solar zenith angles varying from 80 to 82° , just after sunrise at this latitude.

[10] Figure 2 shows the spatial distribution of the measurements. Samples in longitude are consistently $\sim 30^\circ$ apart as the latitude drifts gradually northward from 67.5 to $69.5^\circ N$ during this 12-day span. The longitude sampling overlaps itself such that data from two consecutive days yield about 25 evenly spaced samples over 360° . This increases the effective longitude sampling for data sets that include multiple days of data.

[11] The refractivity data are referenced to surfaces of constant geopotential in order to ensure that the gravity field signature is not confused with atmospheric structure. We analyze zonal refractivity variation with respect to geopotential height, $Z = \Phi/g_0$, where Φ is geopotential and $g_0 = 3.7155 \text{ m s}^{-2}$ is the global average acceleration due to gravity for Mars [Hinson et al., 1999; Andrews et al., 1987, pp. 2–3].

[12] In order to compare results in this paper expressed in terms of geopotential height, Z , with similar results expressed in terms of altitude above a reference geoid, z , we use the approximation,

$$Z(z) \approx R_0^2 \left(\frac{-1}{R_0 + z} + \frac{1}{R_0} \right) = \frac{zR_0}{z + R_0} \quad (1)$$

for a reference radius $R_0 \approx 3.385 \times 10^3$ km. The difference between geopotential height, Z , and altitude, z , is significant

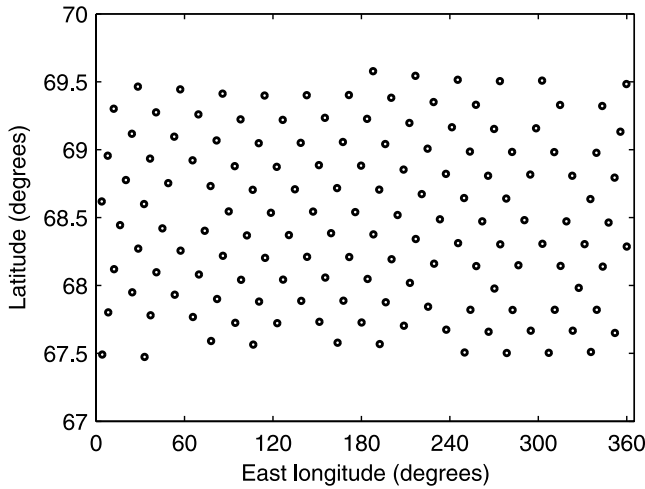


Figure 2. Locations of the 147 MGS refractivity profiles in this data set. Data were acquired in the northern hemisphere from 9 to 21 December 2000, L_S from 87 to 92°, t_{LST} from 2.76 to 2.79 hours, and solar zenith angles from 80 to 82°.

and needs to be accounted for when comparing altitude and geopotential height, e.g., an altitude of 130 km corresponds to a geopotential height of 125 km.

[13] Figure 3 shows a typical profile of refractivity versus geopotential height from this data set. The definition of refractivity, ν , is based on refractive index, μ , such that $\nu = (\mu - 1)$. Refractivity is proportional to both neutral density, n , and electron density, n_e ,

$$\nu \approx \bar{\kappa}n - \kappa_e n_e \quad (2)$$

where $\bar{\kappa}$ is the average molecular refractive volume, $\sim 1.804 \times 10^{-29} \text{ m}^3$ for Mars, and

$$\kappa_e \approx \frac{r_e \lambda_{RS}^2}{2\pi} \quad (3)$$

is a constant dependent on the parameters of the signal transmitted by MGS [Eshleman, 1973]. Here, λ_{RS} is the

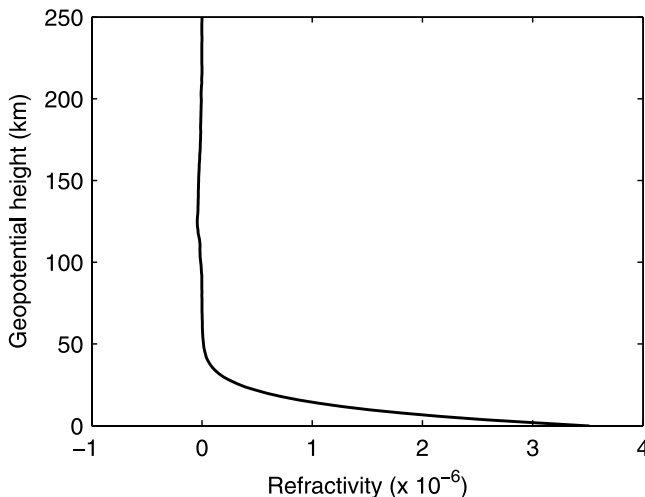


Figure 3. Sample refractivity profile at 67.5°N and 33°E. The vertical resolution is roughly 500 m.

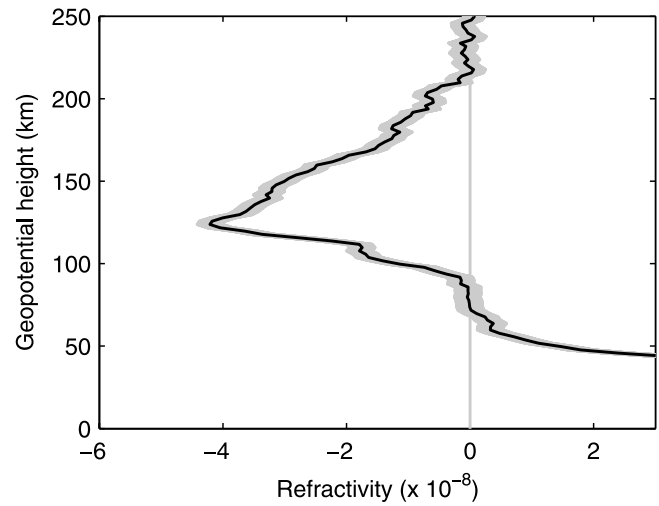


Figure 4. Sample refractivity profile showing the structure of the ionosphere. Shaded envelope gives ± 1 standard deviation experimental error. This profile is the same as in Figure 3, expanded to show the details of the ionosphere.

wavelength of the transmitted radio signal, 3.56 cm, and r_e is the classical (Compton) electron radius, $2.8179 \times 10^{-15} \text{ m}$. As a result of the variation in ionization with altitude, the neutral term, $\bar{\kappa}n$, dominates at lower altitudes, while the plasma term, $\kappa_e n_e$, dominates at higher altitudes. Although $n \gg n_e$ throughout the range of these measurements, a transition in dominance occurs because the plasma coefficient $\kappa_e \approx 5.68 \times 10^{-19} \text{ m}^3$ is many orders of magnitude larger than $\bar{\kappa}$. Note also the negative sign of the plasma term in equation (2).

[14] Figure 4 expands the upper neutral atmosphere and ionosphere from the profile in Figure 3, clearly showing the region above $\sim 75 \text{ km}$ where the refractivity structure changes sign due to the dominance of electron density, that is, where $\bar{\kappa}n \leq \kappa_e n_e$. Note that the combined effect of neutrals and electrons has a comparatively weak contribution to refractivity in the region between 60 and 80 km. Above 80 km, the electron density generally increases with height until the peak at $\sim 130 \text{ km}$, above which n_e generally decreases.

3. Method of Analysis

[15] In this paper, we study zonal refractivity variations at fixed geopotential heights ranging from the surface to 250 km. Figure 5 shows the zonal refractivity variation at three different heights. The zonal mean has been subtracted. Rough wave shapes are discernible in the neutral atmosphere and ionosphere, at the 25 and 125 km levels, respectively. At 50 km, the zonal refractivity variations have a weaker amplitude than those at 25 km and 125 km.

[16] The general expression for an atmospheric wave in refractivity, ν , with respect to east longitude, λ , and true local solar time, t_{LST} , can be written [Forbes and Hagan, 2000; Wilson, 2000]:

$$\nu(\lambda, t_{LST}; Z, \theta, L_S) = \sum_{\sigma, s} A_{\sigma, s}(Z, \theta, L_S) \cdot \cos[(s - \sigma)\lambda + \sigma t_{LST} - \phi_{\sigma, s}(Z, \theta, L_S)] \quad (4)$$

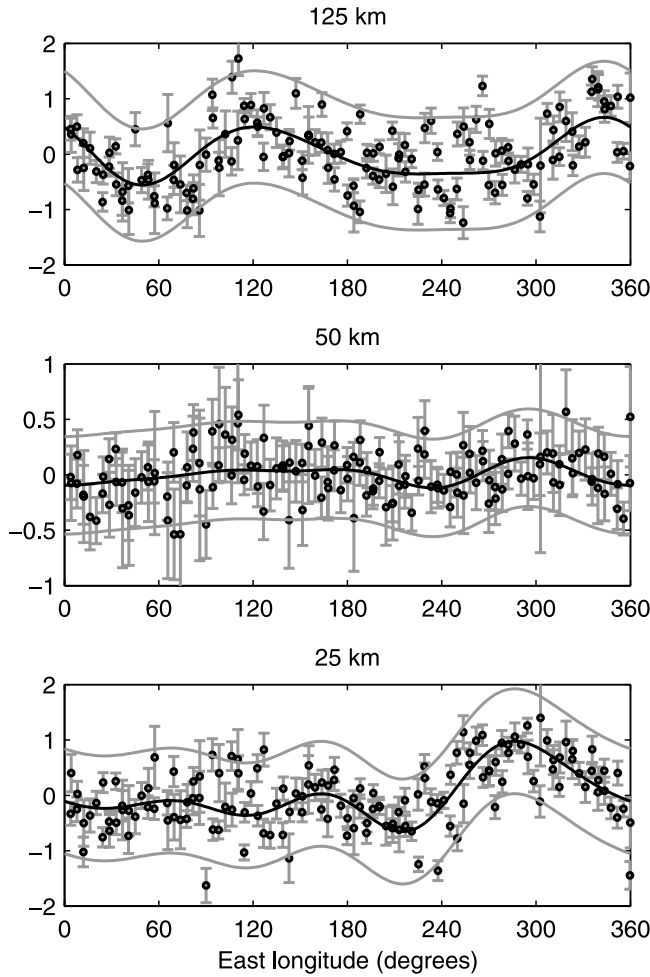


Figure 5. Zonal refractivity variation at geopotential heights of 25, 50, and 125 km. The zonal mean has been subtracted; experimental error bars are ± 1 standard deviation. Panels show the neutral atmosphere (25 km), an intermediate level (50 km), and the ionosphere (125 km). Large-scale structure is more prominent at 25 and 125 km than at 50 km. Curves show results of weighted least squares fits to the original data points using $k = 1-4$ (solid line), as in equation (5). Confidence bounds on the experimental data (outer shaded lines) are at 95% levels. Note the change in vertical scale on Figure 5 (middle).

where Z is height, θ is latitude, L_S is areocentric longitude of the Sun, $A_{\sigma,s}$ is the amplitude, σ is the temporal frequency (e.g., $\sigma = 1$ is diurnal, $\sigma = 2$ is semidiurnal), s is the zonal wave number (e.g., $s = 0$ is zonally uniform, $s = +1$ is westward wave 1, $s = -1$ is eastward wave 1), and $\phi_{\sigma,s}$ is the phase.

[17] Because our observations occur at fixed local time and within narrow bands in both latitude and season, we can simplify the wave equation used to decompose zonal refractivity variations. It is clear from equation (4) that for fixed t_{LST} observations, we can combine the zonal wave number, s , and the temporal frequency, σ , into a single ‘observed wave number,’ $k = |s - \sigma|$. Such an approach means that we cannot uniquely identify either s or σ , however. For example, $k = 2$ could be a stationary wave 2

disturbance ($s = 2, \sigma = 0$), or, it could be an eastward traveling wave 1 diurnal tide ($s = -1, \sigma = 1$). We also can combine the constant σt_{LST} term with the phase to form an apparent ϕ_k . We apply these simplifications to describe zonal refractivity variation as

$$v(\lambda; Z) = \sum_{k=1}^N A_k(Z) \cos[k\lambda - \phi_k(Z)]. \quad (5)$$

We use weighted least squares, with the experimental standard deviation as the weights, to solve for the amplitudes, A_k , and phases, ϕ_k , at geopotential heights from the surface through 250 km in steps of 2 km. In this paper, we consider only $k = 1-4$, although the longitudinal sampling in this data set allows investigation of higher-order observed wave numbers. This method of analysis has been applied previously to radio science data from the neutral atmosphere [e.g., *Hinson et al.*, 2003], but its application to the ionosphere has been limited until now to measurements of the height of the electron density peak [*Bougher et al.*, 2004].

4. Results

[18] We present and discuss our wave decomposition results for both individual k and for the composite of $k = 1-4$. The results are discussed in five subsections: Section 4.1 briefly summarizes the key features of the Martian ionosphere, section 4.2 describes the behavior of ϕ_k in the ionosphere, section 4.3 interprets the unique structure in A_1-A_3 at 80–200 km as vertical displacement of the ionosphere, section 4.4 details the structure of A_k and ϕ_k in the neutral atmosphere, and section 4.5 considers both the separate and the composite longitude-height cross sections for $k = 1-4$ over the entire altitude range.

[19] Figure 5 compares the fit from equation (5) for $k = 1-4$ to the measured zonal refractivity variation at three different geopotential heights. In the neutral atmosphere, at 25 km, the fit captures both the smaller amplitude variations from 0 to 180°E, as well as the large maximum at 285°E. The zonal refractivity variations in the ionosphere, at 125 km, have a similar scale in amplitude to those at 25 km, with maxima at about 120° and 340°E and a well-defined minimum near 50°E. Although trends in zonal refractivity variation at 50 km are weaker in amplitude and have a larger standard deviation compared with the neutral atmosphere and ionosphere, structure is still detectable and represented by the fit.

[20] The individual amplitude and phase terms, with their respective ± 1 experimental standard deviation confidence envelopes, are plotted from the surface to 250 km in Figures 6a–6h. The uncertainty in amplitude is essentially independent of height, such that the measurements are most reliable where the amplitude is relatively large. Small amplitudes are accompanied by larger uncertainties in phase, such as in the transition region at 60–80 km and in the region above 220 km. The amplitude profiles contain distinct maxima and minima at altitudes of 90–150 km, particularly at $k = 2$ and 3, that are discussed further in section 4.3. The amplitudes are largest in the neutral atmosphere at altitudes below about 60 km; this structure is discussed in section 4.4.

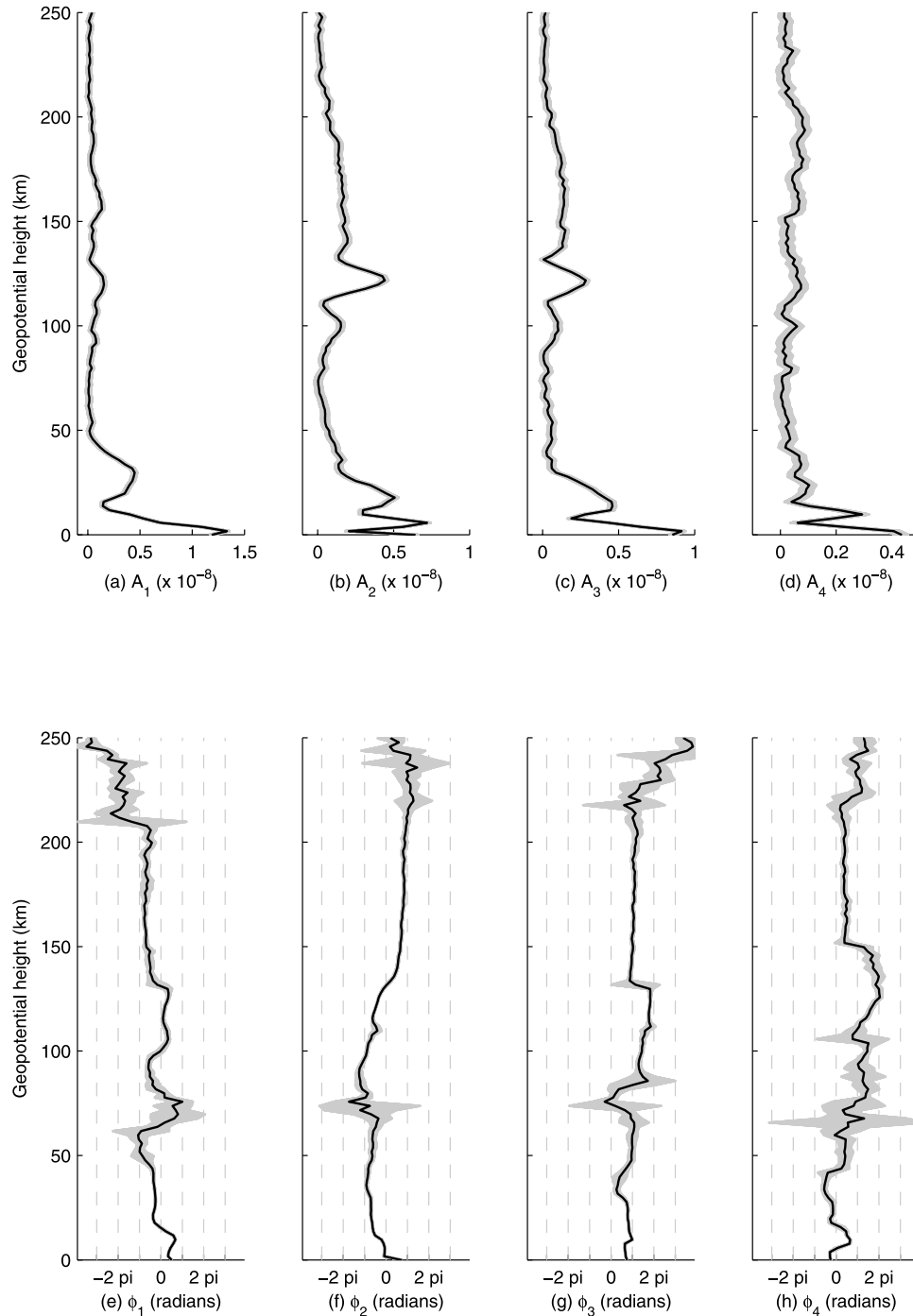


Figure 6. (a)–(d) Amplitudes and (e)–(h) unwrapped phases in radians for $k = 1$ –4. Phase unwrapping changes absolute jumps greater than π to their 2π complement. Both amplitudes and phases are plotted with corresponding ± 1 standard deviation confidence envelopes (shading). Note the change in horizontal scale in Figures 6a–6d. The vertical dashed lines indicate spacing of π .

4.1. Mars Ionosphere

[21] Figure 7 shows the zonal mean refractivity profile, $\bar{\nu}(Z)$, at altitudes above 80 km. The refractivity in this region is dominated by free electrons, as represented by the second term on the right hand side of equation (2), whose sign is negative. The primary electron density peak at ~ 130 km is controlled by photochemical processes and its height is determined by the depth that the solar EUV radiation

penetrates into the atmosphere. The vertical structure of the ionosphere is therefore sensitive to variations in neutral density, such as expansion or contraction [Bougher *et al.*, 2001]. The secondary electron density peak, or shoulder, at ~ 110 km is generated by soft X-ray ionization [Fox *et al.*, 1996; Bougher *et al.*, 2001]. On the topside, around 200 km, the atmospheric scale height and the mean free path for

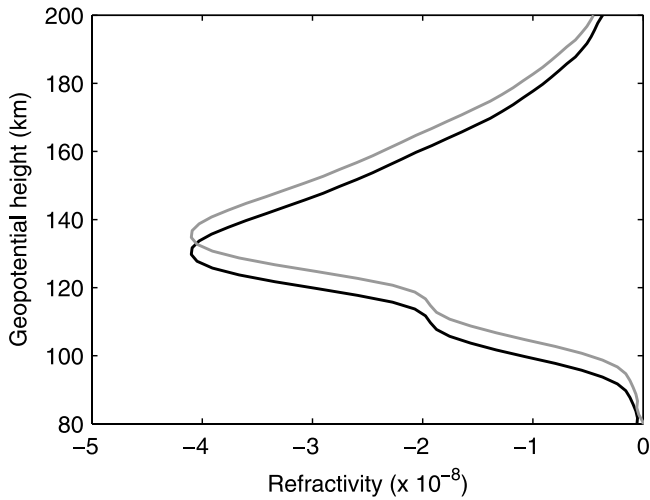


Figure 7. Illustration of ionospheric vertical displacement. The zonal mean refractivity profile (solid line) is shown with an artificial vertical displacement (shaded line) of 5 km.

neutral particles are approximately the same, which defines the base of the exosphere [Martiniš et al., 2003].

4.2. Phase Reversals in the Ionosphere

[22] One of the most noticeable features in the ϕ_k shown in Figures 6e and 6f are the phase reversals (phase shifts of π) in the ionosphere. In the ionosphere, the behavior of ϕ_1 and ϕ_3 are similar, whereas ϕ_2 and ϕ_4 behave much differently. From 100 to 220 km, ϕ_1 and ϕ_3 remain nearly constant with height, except for an abrupt phase reversal at the location of the electron density primary peak at about 130 km. The shift for ϕ_1 and ϕ_3 correlate to the change in the sign of $\partial\bar{v}(Z)/\partial Z$ around the electron density primary peak, which is further discussed in section 4.3. The minor differences between ϕ_1 and ϕ_3 in the ionosphere are that ϕ_1 has a slightly more gradual phase shift with height around the electron density peak, and it also has some small fluctuations beginning at about 100 km and continuing up to ~ 130 km before reversing. On the other hand, ϕ_2 and ϕ_4 do not have much in common. There does not appear to be a sharp phase reversal for ϕ_2 , but rather a gradual drift of roughly π per 50 km as it passes through the electron density primary peak. There are two sharp phase reversals within a 50 km span in the ionosphere for ϕ_4 . The first

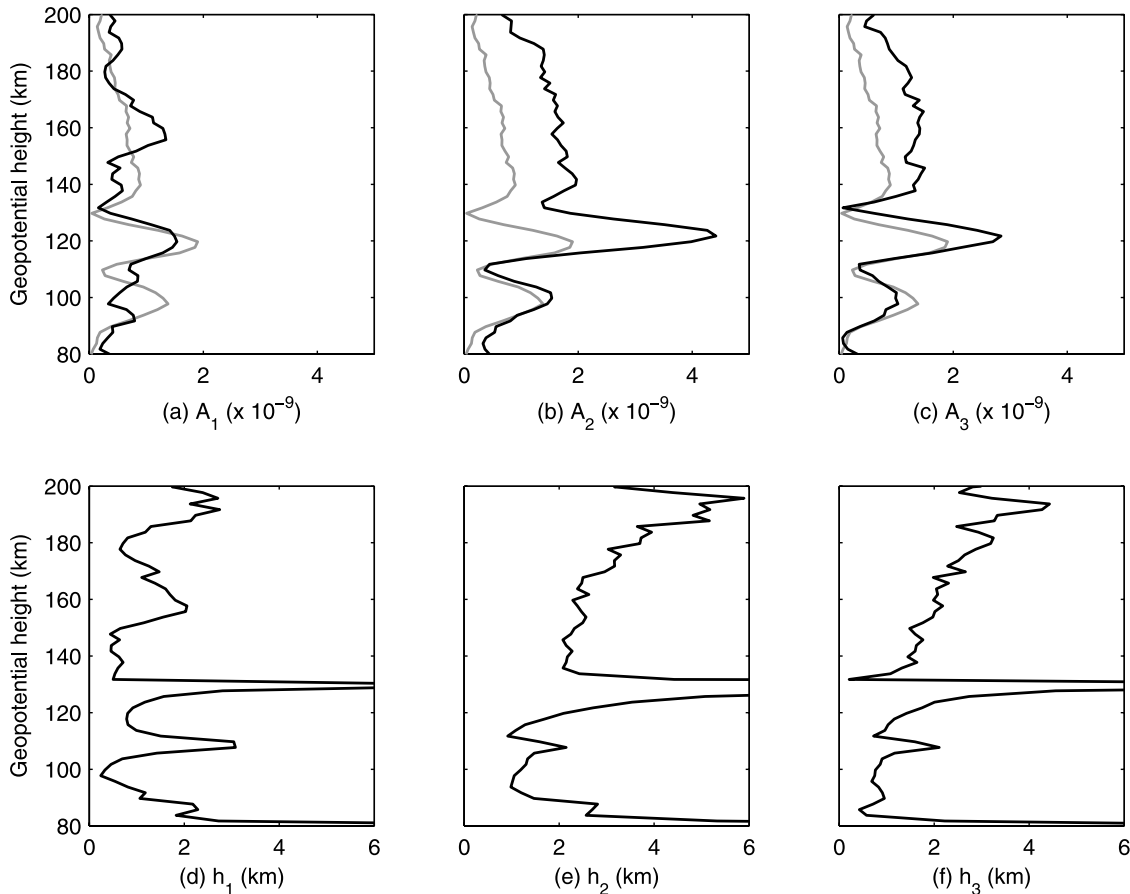


Figure 8. Effects of vertical displacement of the ionosphere. (a–c) Comparison of the A_k (solid line) to the model predictions (shaded line) from equation (6). The similarity between the model and the amplitudes within this altitude range shows that zonal variations of refractivity result from a longitude-dependent vertical displacement of the ionosphere. (d–f) Displacement, h_k , implied by taking the ratio of the measured A_k and the model. A singularity occurs near 130 km, where the model approaches zero.

occurs near the secondary electron density peak (or shoulder) at ~ 110 km. The second phase reversal for ϕ_4 is at ~ 150 km. At altitudes between 150 and 210 km, the ϕ_k have remarkably little variation with height for all k .

[23] To summarize, the phase reversals in ϕ_1 and ϕ_3 correlate with the location of the primary electron density peak, while the first transition in ϕ_4 corresponds to the secondary peak, and ϕ_2 has a comparatively steady rate of change through the ionosphere. This discussion of ϕ_k in the ionosphere is exclusive of the refractively weak transition region from 60 to 80 km, where phases may be shifting more randomly.

4.3. Ionospheric Vertical Displacement

[24] We now show that the distinct maxima-minima structures in A_1 – A_3 from 80 to 200 km in Figure 6 are caused by vertical displacement of the ionosphere. The observations are at fixed local time, within a narrow band of latitude, within a small range of solar zenith angles (80 – 82°), and in solar moderate conditions [Bougher *et al.*, 2004]. We constructed a model for comparison with the $A_k(Z)$ based on the zonal mean refractivity profile for this data set, $\bar{v}(Z)$, as shown in Figure 7.

[25] A small vertical displacement of the zonal mean profile, such as that shown in Figure 7, produces the following change in refractivity:

$$\delta\bar{v}(Z) \equiv \bar{v}(Z) - \bar{v}(Z+h) \approx -h \frac{\partial\bar{v}(Z)}{\partial Z} \quad (6)$$

Figures 8a–8c compare $|h\partial\bar{v}/\partial Z|$ with A_1 – A_3 for an assumed displacement of $h = 1$ km. With this h , there is reasonably good agreement between the model and the observations at all three wave numbers. The model most closely resembles A_3 , where it accounts for all minima and maxima that occur within this altitude range. There is also a striking similarity between the model and A_2 , except that the predicted minimum at 130 km is much deeper than the one observed. For A_1 , the observed minimum at 110 km is not as deep as the one predicted by the model, and the local maximum at 100 km predicted by the model is absent from the observations. This model also accounts for the phase reversals in ϕ_1 and ϕ_3 at the electron density peak, where $\partial\bar{v}/\partial Z$ changes sign.

[26] The results in Figures 8a–8c imply that a model in which h varies with height would produce a better fit to the observations. At each zonal wave number, we solved for $h_k(Z)$ by computing the ratio of A_k to $|\partial\bar{v}/\partial Z|$. The results appear in Figures 8d–8f. This method produces plausible results over most of this altitude range, although it breaks down predictably near the height of the electron density peak, where $|\partial\bar{v}/\partial Z|$ goes to zero, resulting in a singularity in h_k .

[27] In Figure 8d, h_1 fluctuates with altitude with an average value of ~ 1 km, while Figures 8e–8f show that both h_2 and h_3 generally increase with altitude (apart from the singularities at 130 km). The value of h_2 increases from ~ 1 km at 100 km altitude to ~ 4 km at 180 km. The results for h_3 resemble those for h_2 except that the magnitude of the vertical displacement is reduced by about 25% at $k = 3$. At an altitude of 135 km, just above the singularity, h_2 is ~ 2 km and h_3 is ~ 1.5 km.

[28] Bougher *et al.* [2001, 2004] previously analyzed the electron density profiles produced by the MGS radio science experiments, focusing primarily on characterizing zonal variations in the height of peak electron density. Figure 3 of Bougher *et al.* [2004] shows results derived from the same subset of data used here, which can be compared with our results at 125 km in Figure 5 (top). Both plots show similar patterns of zonal variation, with prominent upward displacements of the ionosphere near 120°E and 340°E , and a well-defined downward displacement near 50°E . Our estimates for the magnitude of these displacements are roughly 30% smaller than the values reported by Bougher *et al.* [2004], but this level of agreement is probably within the uncertainties of the two methods of analysis. In addition to confirming the results reported by Bougher *et al.* [2004], our method of analysis also extends the characterization of ionospheric structure to altitudes well above and below the electron density peak.

[29] Figure 9 shows a longitude-height cross section of the observed refractivity field for $k = 3$, illustrating the distinctive spatial modulation of ionospheric structure. These observations are consistent with a longitude-dependent vertical displacement of the ionosphere, which accounts for the locations of the maxima and minima in amplitude as well as the abrupt phase reversal at the electron density peak. This ionospheric behavior implies the presence of $k = 3$ variation in the neutral density with a large vertical wavelength. Such modulation of neutral density would control the height at which the ionosphere forms.

[30] An eastward propagating semidiurnal tide with zonal wave number 1 ($s = -1$, $\sigma = 2$) is probably responsible for this $k = 3$ modulation of ionospheric structure. Direct support for this conclusion can be found in several previous investigations, such as through comparisons between zonal variations in the height of peak electron density measured by MGS radio occultations and zonal variations in neutral density measured by the MGS accelerometer [Bougher *et al.*, 2001]. In addition, Withers *et al.* [2003] used classical tidal theory to identify the $s = -1$, $\sigma = 2$, $n = 1$ Hough mode as a major contributor to the prominent $k = 3$ density variations that appear in MGS accelerometer measurements. Finally, this tidal component is a prominent, recurring feature of numerical simulations at the latitude, altitude, and general season of the measurements considered here, including those conducted with the GFDL MGCM [Wilson, 2002, Figure 3], the LMD MGCM [Angelats *i Coll et al.*, 2004, Figure 5], and the ARC MGCM coupled with the MTGCM [Bougher *et al.*, 2004, Figure 10].

[31] The results in Figures 8a and 8b also suggest that tides are responsible for the refractivity structure at $k = 1$ and $k = 2$ in the ionosphere. Candidates for explaining the $k = 2$ structure at the latitude, altitude, and season of these measurements include an eastward propagating diurnal tide with zonal wave number 1 ($s = -1$, $\sigma = 1$) and a zonally symmetric semidiurnal tide ($s = 0$, $\sigma = 2$) [Angelats *i Coll et al.*, 2004, Figures 4 and 5]. The structure at $k = 1$ may be due to a zonally uniform diurnal tide ($s = 0$, $\sigma = 1$) [Angelats *i Coll et al.*, 2004, Figure 4].

4.4. Neutral Atmosphere

[32] We now consider the wave decomposition results for the lower neutral atmosphere, shown in Figures 6 and 10.

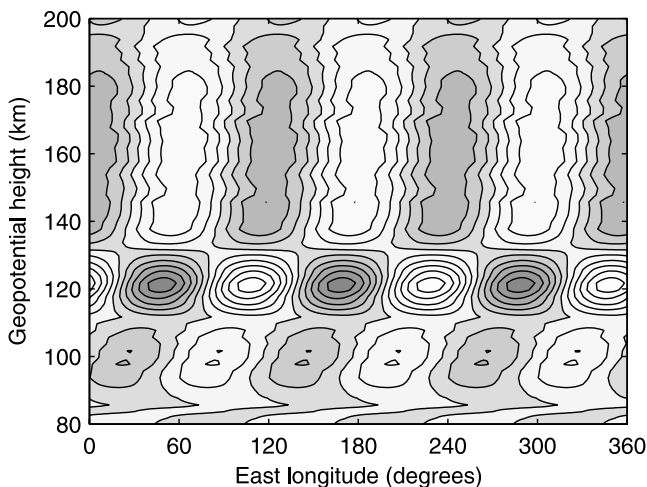


Figure 9. Refractivity field for $k = 3$. Amplitude signature is unique and indicative of zonal modulation in the height of the ionosphere. Contours are shown at $0, \pm 0.5, \pm 1, \pm 1.5, \pm 2, \pm 2.5,$ and $\pm 3 \times 10^{-9}$. Shaded areas indicate negative amplitude, and white areas indicate positive amplitude. Note the presence of an abrupt phase reversal at ~ 130 km, the height of peak electron density.

There is significant structure in amplitude for $k = 1-4$ at altitudes below 60 km. At each of these observed wave numbers, there are local maxima in amplitude structure between the surface and 50 km in altitude. As k increases, the amplitude structure is confined to a progressively shallower layer near the surface, as shown in Figure 10, consistent with the general behavior expected for stationary Rossby waves [Andrews *et al.*, 1987, section 4.5.2]. Although the layer width decreases with increasing k , for A_1-A_3 , the magnitudes of the local maxima remain fairly constant at $\sim 5 \times 10^{-9}$ as shown in Figure 6. Compared to A_1-A_3 , the magnitude of the local maximum decreases by about a factor of two for A_4 . The local maximum for A_1 is at 30 km, with structure extending from the surface to 50 km, above the range of the standard retrieved temperature and pressure profiles. A_2 has two elevated local maxima, the upper one at ~ 18 km and the lower at ~ 6 km. A_3 and A_4 each have a single elevated local maximum at ~ 15 km and ~ 10 km, respectively.

[33] There is also a correlation between phase shifts and the amplitude structure around the local maxima. For each ϕ_k , there is a shift in phase both below and above each elevated amplitude maximum (Figures 6 and 10). For ϕ_1 , there are detectable shifts of π at about 12 km and 40 km. For $k = 2$, which has two elevated local maxima, there is a strong shift of π from the surface to 2 km, and two weaker shifts of about $\pi/2$ at 10 km and 30 km. The phase for $k = 3$ shifts by $\pi/2$ at about 8 km and 28 km, and ϕ_4 shifts by π at about 4 km and 16 km.

[34] The elevated maxima seen in A_1-A_4 in the neutral atmosphere in Figure 6 are consistent with results from two recent papers, one based on experimental data and one based on simulation. Working with the LMD MGCM, Figure 9 of Angelats *i Coll et al.* [2004] showed increases in neutral density on the order of 1% for stationary waves $s = 1-3$ from ~ 20 to 50 km at a slightly earlier season ($L_s = 65^\circ$) and same

latitude, $\sim 70^\circ\text{N}$, as the data set presented here. In the MGS data set, the mean refractivity value is $\sim 3.9 \times 10^{-7}$ at 25 km, the region where A_1 has its local maxima. When compared with the observed 5×10^{-9} local maxima of A_1 , we calculate a $\sim 1.3\%$ increase in refractivity for this region. A similar increase of ~ 1 K in temperature, about 0.5%, is seen in Figure 9 of Banfield *et al.* [2003], who characterizes stationary waves using the MGS TES nadir data at high northern latitudes around the summer solstice and at pressure levels between 6.1 and 0.8 mbar. We note that the TES nadir data are averaged both diurnally and over three times as long a span in L_s as the refractivity data set, and have a vertical resolution of roughly a scale height.

[35] Given the above discussion and comparison with both TES observations and model results, the observed structure in the lower neutral atmosphere that appears in Figures 6 and 10 is likely due to stationary waves. The refractivity data are useful for both providing improved characterization of stationary waves in northern late spring and early summer and for validating MGCM simulations.

4.5. From the Surface to 250 km

[36] One key attribute of the MGS radio occultation refractivity measurements is the ability to study the entire range from the surface through 250 km. In addition to the examples already discussed for separate k , Figure 10 provides additional information for individual wave numbers from the surface to 250 km. For example, there is a visible transition region, in that there appear to be primarily stationary waves below ~ 75 km, and primarily thermal tides above ~ 75 km.

[37] Figure 10 also shows more clearly how the wave structure behaves with respect to longitude. Specifically, the shifts seen in ϕ_k in Figures 6e–6h translate into eastward or westward tilts in the wave structure in Figure 10. There is a general westward tilt for $k = 1$ above 20 km and below 180 km. For $k = 2$, the trend is westward in the neutral atmosphere and eastward from the transition region to 220 km. The behavior at $k = 3$ in the ionosphere is almost constant (with a slight eastward tilt), although in the neutral atmosphere it is more variable. In the neutral atmosphere, $k = 4$ appears to have a slight westward tilt below 40 km, above which it becomes eastward into the transition region. The tilt for $k = 4$ reverses around the electron density peak, eastward below and westward above, and then remains constant from 150 to about 220 km. For all k , the variability of the tilt becomes more random in the transition region.

[38] At the upper limit of the refractivity profile between 200 and 240 km, as shown in Figure 6, the A_k decrease in amplitude by at least a factor of two (A_1), and sometimes by as much as an order of magnitude (A_3). There is also a significant increase in the phase error envelope above 220 km. This is probably due to increased noisiness of the signal as changes due to atmospheric refractivity become smaller. This also implies that wave decomposition does not capture the behavior of the ionosphere at this altitude as well as it does below 220 km, although Figure 11 hints at some semblance of structure in that altitude range. At 200 km, as mentioned in section 4.1, the scale height of the Martian atmosphere and mean free path are comparable [Mendillo *et al.*, 2003; Martinis *et al.*, 2003]. There are also changes in the composition of the atmosphere within this

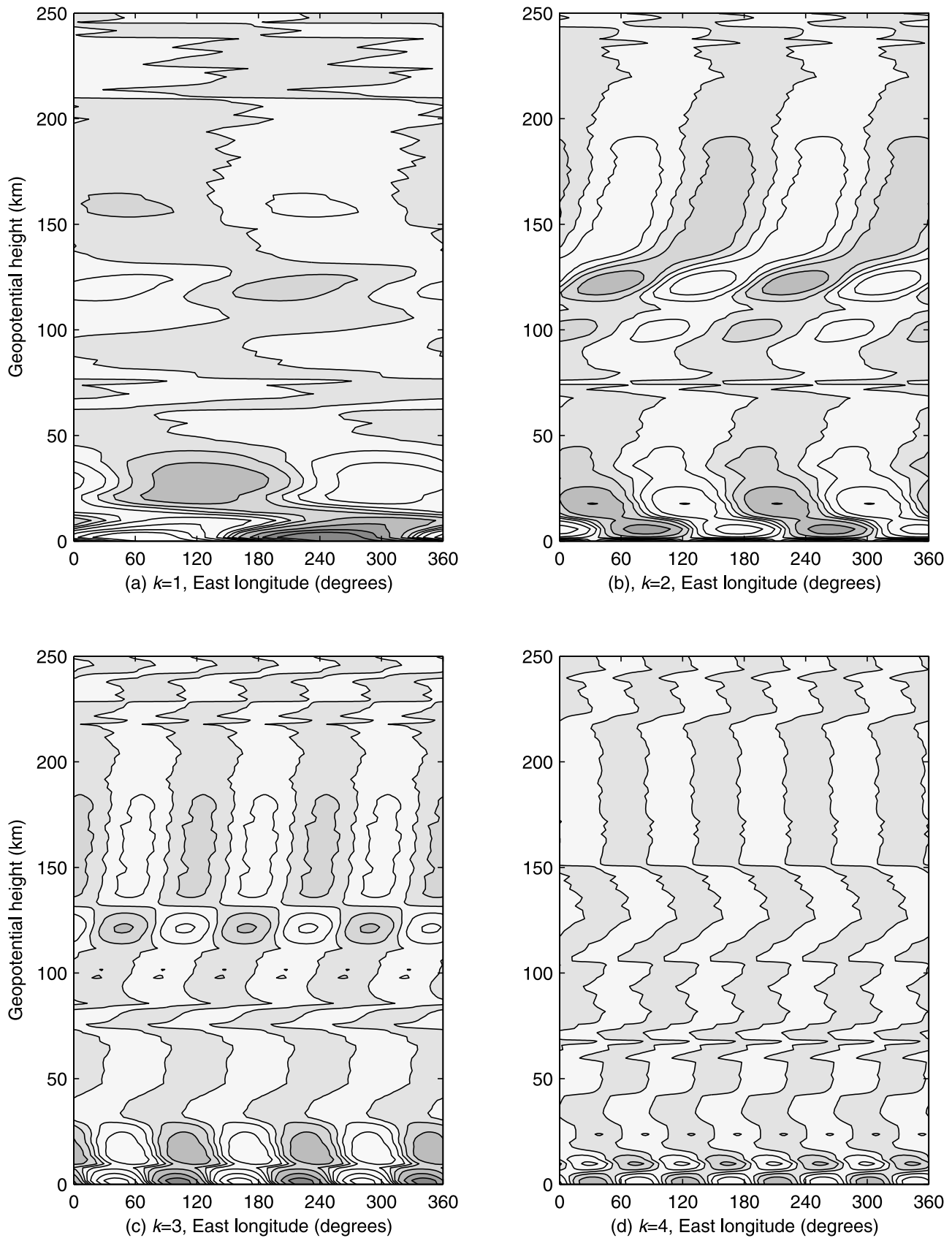


Figure 10. Observed refractivity field from 0 to 250 km: (a) $k = 1$, (b) $k = 2$, (c) $k = 3$, and (d) $k = 4$. Contours are shown at $0, \pm 1, \pm 2.5, \pm 5, \pm 7.5$, and $\pm 10 \times 10^{-9}$. Shaded areas indicate negative amplitude, and white areas indicate positive amplitude.

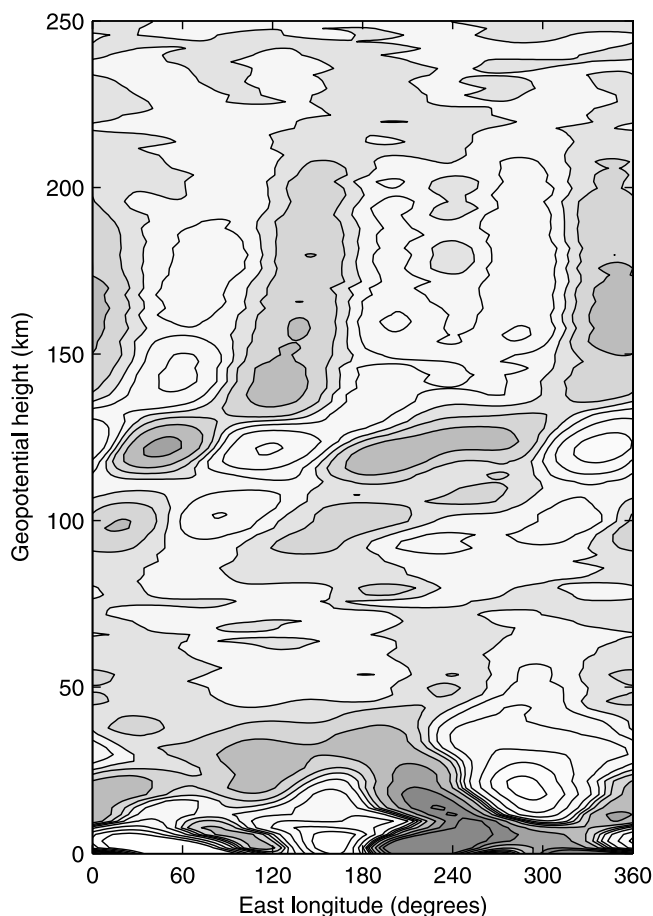


Figure 11. Total refractivity field for the summation of $k = 1-4$ from 0 to 250 km. Contours are shown at 0, ± 1 , ± 2.5 , ± 5 , ± 7.5 , and $\pm 10 \times 10^{-9}$. Shaded areas indicate negative amplitude, and white areas indicate positive amplitude.

altitude range to consider. For example, a change in dominance from CO_2 to O has been modeled and shown to vary in strength and altitude (200–240 km) with solar activity level [Fox *et al.*, 1996, Figure 1]. The decrease in amplitude and increase in the fit error envelopes seen in refractivity above this altitude may be due to noise alone or due to a combination of noise plus a physical change in the atmosphere.

[39] Figure 11 shows the composite of all four wave numbers from Figure 10, showing the refractivity structure from the surface to 250 km in the Martian northern hemisphere around summer solstice. The features in Figure 11 are due to the constructive and destructive interference between each of the individual wave numbers. For example, the increase in refractivity in the neutral atmosphere at 300°E and between 10 and 50 km is largely due to the constructive interference among $k = 1-3$.

5. Conclusions

[40] The results in this paper demonstrate a new method of using the raw refractivity profiles from the MGS radio science experiment to characterize the structure of the Martian atmosphere over an extended altitude range, from the surface to 250 km. A weighted least squares analysis of

zonal refractivity variation reveals structure in amplitude and phase with altitude for observed wave numbers 1–4. Specific examples of structure in the neutral atmosphere and ionosphere confirm and extend results from previous analyses and simulations.

[41] In the ionosphere, phase reversals seen in ϕ_1 and ϕ_3 are correlated with the location of the electron density peak, where the slope of the mean refractivity profile changes sign. Although ϕ_2 and ϕ_4 do not change phase as rapidly around the electron density peak, ϕ_2 has a constant phase progression of π every ~ 50 km in the ionosphere, and ϕ_4 appears to be sensitive to the secondary peak.

[42] Our analysis using refractivity profiles demonstrates that the structure of the Martian ionosphere contains the signature of thermal tides for $k = 1-3$, with a signature that is particularly distinct for $k = 3$. The amount of ionospheric vertical displacement appears to increase with altitude from ~ 90 to 190 km for $k = 2$ and $k = 3$, with corresponding h_2 of ~ 2 km and h_3 of ~ 1.5 km at the electron density peak ~ 130 km.

[43] Analyses by Bougher *et al.* [2001, 2004], Wilson [2002], Withers *et al.* [2003], and Angelats i Coll *et al.* [2004] indicate that the strong variations in observed wave number 3 are the result of an eastward propagating semidiurnal tide. In addition, they suggest that variations in our observed wave number 2 are due to the combined effect of an eastward propagating diurnal period zonal wave number 1 component and a zonally uniform semidiurnal component. Variations in observed wave number 1 are probably due to a zonally uniform diurnal component.

[44] In the neutral atmosphere, as k increases, the width of the wave structure in altitude decreases, which supports their identification as stationary Rossby waves. Increases seen in amplitude between the surface and 50 km for A_1-A_4 are similar to stationary wave results from both an LMD MGC simulation and analysis of MGS TES nadir measurements at a similar latitude and season [Angelats i Coll *et al.*, 2004; Banfield *et al.*, 2003].

[45] In Figure 10, there appears to be a distinct separation between a region of stationary waves in the neutral atmosphere (surface to ~ 75 km) and tidal modes in the upper neutral atmosphere and ionosphere (above ~ 75 km). On the upper limit of the refractivity profiles, between 200 and 240 km, there is a noticeable decrease in amplitude for all A_k , and increase in the error envelope for all ϕ_k .

[46] The refractivity data cover altitude ranges pertinent to future mission aerobraking, aerocapture, and entry, descent, and landing (EDL) [Beatty *et al.*, 2005]. Further analysis of MGS refractivity data sets in geographical regions being considered for landing sites would provide a useful planning resource.

[47] We conclude that refractivity profiles can be used to examine Martian atmospheric structure at altitude ranges that extend beyond the vertical range of standard temperature, pressure, and electron density profiles. While atmospheric contributions to refractivity are weaker in the transition region between the neutral atmosphere and the ionosphere, new and useful information can still be extracted from a refractivity profile data set using weighted least squares wave decomposition. We anticipate that in future work, including the study of larger data sets and collaboration and comparison with computational models,

refractivity profiles will continue to make significant contributions to understanding the Martian atmosphere.

[48] **Acknowledgments.** We thank those supporting the Mars Global Surveyor mission at all levels. In particular, we thank the Deep Space Network, the Radio Science Systems Group at JPL, and the MGS Radio Science Team, especially R. Simpson, J. Twicken, and R. Jackson. We also thank two anonymous reviewers for their useful and constructive comments for improving this manuscript.

References

- Andrews, D. G., J. R. Holton, and C. B. Leovy (1987), *Middle Atmosphere Dynamics*, 489 pp., Elsevier, New York.
- Angelats i Coll, M., F. Forget, M. A. Lopez-Valverde, P. L. Read, and S. R. Lewis (2004), Upper atmosphere of Mars up to 120 km: Mars Global Surveyor accelerometer data analysis with the LMD general circulation model, *J. Geophys. Res.*, *109*, E01011, doi:10.1029/2003JE002163.
- Angelats i Coll, M., F. Forget, M. A. Lopez-Valverde, and F. Gonzalez-Galindo (2005), The first Mars thermospheric general circulation model: The Martian atmosphere from the ground to 240 km, *Geophys. Res. Lett.*, *32*, L04201, doi:10.1029/2004GL021368.
- Banfield, D., B. J. Conrath, M. D. Smith, P. R. Christensen, and R. J. Wilson (2003), Forced waves in the Martian atmosphere from MGS TES nadir data, *Icarus*, *161*, 319–345, doi:10.1016/S0019-1035(02)00044-1.
- Banfield, D., B. J. Conrath, P. J. Gierasch, R. J. Wilson, and M. D. Smith (2004), Traveling waves in the Martian atmosphere from MGS TES nadir data, *Icarus*, *170*, 365–403, doi:10.1016/j.icarus.2004.03.015.
- Beatty, D., K. Snook, C. Allen, D. Eppler, W. Farrell, J. Heldmann, P. Metzger, L. Peach, S. Wagner, and C. Zeitlin (2005), An analysis of the precursor measurements of Mars needed to reduce the risk of the first human missions to Mars, report, Mars Exploration Program Analysis Group, Pasadena, Calif., 2 June. (Available at <http://mepag.jpl.nasa.gov/reports/index.html>)
- Bougher, S. W., S. Engel, R. G. Roble, and B. Foster (1999), Comparative terrestrial planet thermospheres: 2. Solar cycle variation of global structure and winds at equinox, *J. Geophys. Res.*, *104*, 16,591–16,611.
- Bougher, S. W., S. Engel, R. G. Roble, and B. Foster (2000), Comparative terrestrial planet thermospheres: 3. Solar cycle variation of global structure and winds at solstices, *J. Geophys. Res.*, *105*, 17,669–17,692.
- Bougher, S. W., S. Engel, D. P. Hinson, and J. M. Forbes (2001), Mars Global Surveyor Radio Science electron density profiles: Neutral atmosphere implications, *Geophys. Res. Lett.*, *28*(16), 3091–3094.
- Bougher, S., S. Engel, D. Hinson, and J. Murphy (2004), MGS Radio Science electron density profiles: Interannual variability and implications for the Martian neutral atmosphere, *J. Geophys. Res.*, *109*, E03010, doi:10.1029/2003JE002154.
- Eshleman, V. (1973), The radio occultation method for the study of planetary atmospheres, *Planet Space Sci.*, *21*, 1521–1531.
- Fjeldbo, G., A. J. Kliore, and V. R. Eshleman (1971), The neutral atmosphere of Venus as studied with the Mariner V Radio Occultation Experiment, *Astron. J.*, *76*(2), 123–140.
- Forbes, J. M., and M. E. Hagan (2000), Diurnal Kelvin wave in the atmosphere of Mars: Towards an understanding of “stationary” density structures observed by the MGS accelerometer, *Geophys. Res. Lett.*, *27*, 3564–3566.
- Forbes, J., A. Bridger, S. Bougher, M. Hagan, J. Hollingsworth, G. Keating, and J. Murphy (2002), Nonmigrating tides in the thermosphere of Mars, *J. Geophys. Res.*, *107*(E11), 5113, doi:10.1029/2001JE001582.
- Forget, F., F. Hourdin, R. Fournier, C. Hourdin, O. Talagrand, M. Collins, S. Lewis, P. Read, and J. P. Huot (1999), Improved general circulation models of the Martian atmosphere from the surface to above 80 km, *J. Geophys. Res.*, *104*, 24,155–24,175.
- Fox, J. L., P. Zhou, and S. W. Bougher (1996), The Martian thermosphere/ionosphere at high and low solar activities, *Adv. Space Res.*, *17*(11), 203–218.
- Gonzalez-Galindo, F., M. A. Lopez-Valverde, M. Angelats i Coll, and F. Forget (2005), Extension of a Martian general circulation model to thermospheric altitudes: UV heating and photochemical models, *J. Geophys. Res.*, *110*, E09008, doi:10.1029/2004JE002312.
- Hinson, D. P., and R. J. Wilson (2004), Temperature inversions, thermal tides, and water ice clouds in the Martian tropics, *J. Geophys. Res.*, *109*, E01002, doi:10.1029/2003JE002129.
- Hinson, D. P., R. A. Simpson, J. D. Twicken, and G. L. Tyler (1999), Initial results from radio occultation measurements with Mars Global Surveyor, *J. Geophys. Res.*, *104*, 26,997–27,012.
- Hinson, D. P., R. J. Wilson, M. D. Smith, and B. J. Conrath (2003), Stationary planetary waves in the atmosphere of Mars during southern winter, *J. Geophys. Res.*, *108*(E1), 5004, doi:10.1029/2002JE001949.
- Hinson, D. P., M. D. Smith, and B. J. Conrath (2004), Comparison of atmospheric temperatures obtained through infrared sounding and radio occultation by Mars Global Surveyor, *J. Geophys. Res.*, *109*, E12002, doi:10.1029/2004JE002344.
- Keating, G. M., et al. (1998), The structure of the upper atmosphere of Mars: In situ accelerometer measurements from Mars Global Surveyor, *Science*, *279*, 1672–1676.
- Krymskii, A. M., T. K. Breus, N. F. Ness, D. P. Hinson, and D. I. Bojkov (2003), Effect of crustal magnetic fields on the near terminator ionosphere at Mars: Comparison of in situ magnetic field measurements with the data of radio science experiments on board Mars Global Surveyor, *J. Geophys. Res.*, *108*(A12), 1431, doi:10.1029/2002JA009662.
- Martinis, C., J. Wilson, and M. Mendillo (2003), Modeling day-to-day ionospheric variability on Mars, *J. Geophys. Res.*, *108*(A10), 1383, doi:10.1029/2003JA009973.
- Mendillo, M., S. Smith, J. Wroten, and H. Rishbeth (2003), Simultaneous ionospheric variability on Earth and Mars, *J. Geophys. Res.*, *108*(A12), 1432, doi:10.1029/2003JA009961.
- Pearl, J. C., M. D. Smith, B. J. Conrath, and P. R. Christensen (2001), Observations of Martian ice clouds by the Mars Global Surveyor Thermal Emission Spectrometer: The first Martian year, *J. Geophys. Res.*, *106*, 12,325–12,338.
- Pollack, J. B., R. M. Haberle, J. R. Murphy, J. Schaeffer, and H. Lee (1990), Simulations of the general circulation of the Martian atmosphere: 1. Polar processes, *J. Geophys. Res.*, *95*, 1447–1473.
- Smith, M. D. (2004), Interannual variability in TES atmospheric observations of Mars during 1999–2003, *Icarus*, *167*, 148–165, doi:10.1016/j.icarus.2003.09.010.
- Smith, M. D., J. C. Pearl, B. J. Conrath, and P. R. Christensen (2001a), One Martian year of atmospheric observations by the Thermal Emission Spectrometer, *Geophys. Res. Lett.*, *28*, 4263–4266.
- Smith, M. D., J. C. Pearl, B. J. Conrath, and P. R. Christensen (2001b), Thermal Emission Spectrometer results: Mars atmospheric thermal structure and aerosol distribution, *J. Geophys. Res.*, *106*, 23,929–23,945.
- Wilson, R. J. (2000), Evidence for diurnal period Kelvin waves in the Martian atmosphere from Mars Global Surveyor TES data, *Geophys. Res. Lett.*, *27*, 3889–3892.
- Wilson, R. J. (2002), Evidence for nonmigrating thermal tides in the Mars upper atmosphere from the Mars Global Surveyor Accelerometer Experiment, *Geophys. Res. Lett.*, *29*(7), 1120, doi:10.1029/2001GL013975.
- Wilson, R. J., and K. Hamilton (1996), Comprehensive model simulation of the thermal tides in the Martian atmosphere, *J. Atmos. Sci.*, *53*(9), 1290–1326, doi:10.1175/1520-0469(1996)053.
- Withers, P., S. W. Bougher, and G. M. Keating (2003), The effects of topographically-controlled thermal tides in the Martian upper atmosphere as seen by the MGS accelerometer, *Icarus*, *164*, 14–32, doi:10.1016/S0019-1035(03)00135-0.
- Withers, P., M. Mendillo, H. Rishbeth, D. P. Hinson, and J. Arkan-Hamed (2005), Ionospheric characteristics above Martian crustal magnetic anomalies, *Geophys. Res. Lett.*, *32*, L16204, doi:10.1029/2005GL023483.

K. L. Cahoy, D. P. Hinson, and G. L. Tyler, Department of Electrical Engineering, Stanford University, STAR Laboratory, 350 Serra Mall, Stanford, CA 94305, USA. (kcahoy@stanford.edu)